PHOTONICS Research

Superior single-mode lasing in a self-assembly CsPbX₃ microcavity over an ultrawide pumping wavelength range

Guoen Weng,[1,5,†] (iD) Jiyu Yan,[1,†] Shengjie Chen,[1,†] Chunhu Zhao,[1,†] Hanbing Zhang,[1] Jiao Tian,[1] Yuejun Liu,[1] Xiaobo Hu,[1] Jiahua Tao,[2] Shaoqiang Chen,[1,2,3,6] (iD) Ziqiang Zhu,[1] Hidefumi Akiyama,[4] and Junhao Chu[1,2]

[1]Department of Electronic Engineering, East China Normal University, Shanghai 200241, China
[2]Ministry of Education Nanophotonics & Advanced Instrument Engineering Research Center, East China Normal University, Shanghai 200241, China
[3]Shanghai Institute of Intelligent Electronics & Systems, Fudan University, Shanghai 200433, China
[4]Institute for Solid State Physics, The University of Tokyo, 5-1-5 Kashiwanoha, Kashiwa, Chiba 277-8581, Japan
[5]e-mail: egweng@ee.ecnu.edu.cn
[6]e-mail: sqchen@ee.ecnu.edu.cn

All-inorganic perovskite micro/nanolasers are emerging as a class of miniaturized coherent photonic sources for many potential applications, such as optical communication, computing, and imaging, owing to their ultracompact sizes, highly localized coherent output, and broadband wavelength tunability. However, to achieve single-mode laser emission in the microscale perovskite cavity is still challenging. Herein, we report unprecedented single-mode laser operations at room temperature in self-assembly CsPbX₃ microcavities over an ultrawide pumping wavelength range of 400–2300 nm, covering one- to five-photon absorption processes. The superior frequency down- and upconversion single-mode lasing manifests high multiphoton absorption efficiency and excellent optical gain from the electron–hole plasma state in the perovskite microcavities. Through direct compositional modulation, the wavelength of a single-mode CsPbX₃ microlaser can be continuously tuned from blue-violet to green (427–543 nm). The laser emission remains stable and robust after long-term high-intensity excitation for over 12 h (up to 4.3×10^7 excitation cycles) in the ambient atmosphere. Moreover, the pump-wavelength dependence of the threshold, as well as the detailed lasing dynamics such as the gain-switching and electron–hole plasma mechanisms, are systematically investigated to shed insight into the more fundamental issues of the lasing processes in CsPbX₃ perovskite microcavities. © 2020 Chinese Laser Press

https://doi.org/10.1364/PRJ.409884

1. INTRODUCTION

Miniaturization and integration of photonic components hold great promise for advancing the field of optoelectronics [1–3]. There has been a long-standing and continuous pursuit of highly stable, wavelength-tunable semiconductor lasers on the micro/nanoscale due to the rapid progress of optical integrated systems. In particular, semiconductor lasers oscillating at a single frequency, such as single-mode lasers, have attracted great interest due to their potential for commercial applications in on-chip optical interconnects [4], quantum information processing [5,6], sensing [7,8], super-resolution imaging [9,10], and ultradense data storage [11]. Over the past decades, a wide range of micro/nanowire lasers has been reported, consisting of a multitude of compositions including various II-VI

and III-V compound semiconductors [12]. Unfortunately, synthesis of these nanowires commonly requires expensive high-temperature or low-pressure conditions. Moreover, although most of these materials are stable in ambient atmosphere, only a few of them have demonstrated broad wavelength tunability, and the so-called "green gap" problem has not been solved in these material systems. Recently, studies on miniaturized lasers from perovskite semiconductors have experienced explosive growth and have led to great advances in lasing performance due to their high optical gain and tunable luminescence over the whole visible wavelength range [13–31]. From a historical perspective, Xing *et al.* reported low-threshold room-temperature (RT) amplified spontaneous emission in perovskite films in 2014 [32]. At almost the same time, lasing from perovskite-based vertical cavity surface emitting

architecture was observed by Deschler *et al.* [16]. Shortly afterwards, Zhang *et al.* achieved near-infrared whispering-gallery-mode (WGM) nanolasers based on perovskite nanoplates [13], while Zhu *et al.* observed high-quality-factor Fabry–Perot (FP) lasing in perovskite nanowires with ultralow threshold of $220 \ nJ/cm^2$ [14]. By conformally coating perovskite film on a silica microsphere, Sutherland and co-workers also demonstrated WGM lasers [15]. Besides, amplified spontaneous emission and lasing from colloidal nanocrystals of cesium lead halide perovskites were realized during nearly the same period by Yakunin *et al.* [33]. Since then, the lead halide perovskite micro/nanostructures served as gain materials with tunable lasing wavelengths that have been dramatically developed. Very recently, Qin *et al.* reported the first stable quasi-2D perovskite lasers under continuous-wave optical pumping in air at RT [34], which is expected to pave the way to the realization of future current-injection perovskite lasers. Huang *et al.* demonstrated the ultrafast control of perovskite-based vortex microlasers with ultralow energy consumption and simultaneously ultrahigh speed [35], providing a route to develop high-speed classical and quantum communication systems. Compared to organic and organic–inorganic perovskite components, all-inorganic cesium lead halide perovskites ($CsPbX_3$, X = Cl, Br, I, or their mixture) present better physical and chemical stability with respect to temperature, moisture, and light exposure, representing promising prospects of $CsPbX_3$ perovskites for the development of stable and high-performance devices [36,37]. Indeed, perovskite lasers have been achieved in many micro/nanostructures with different geometries, such as micro/nanowires [14,17–20,24,38,39], nanoplatelets [13,21,22,40], microspheres [15,23], microcubes [25,41,42], and hemispheres [27], for both single- and multiphoton excitations. However, most of these microcavity lasers are subject to random fluctuations and instabilities, showing typical multimode lasing. In principle, multiple modes in a resonant cavity are competitive with each other, and the one with the highest gain will dominate, but inhomogeneous gain saturation caused by spatial hole burning or crystal/cavity inhomogeneity can sustain multiple lasing modes [14,43]. Despite the extensive efforts that have been devoted to this enterprise, the realization of single-mode lasing in a $CsPbX_3$ microcavity with narrow spectral linewidth and broadband tunability remains a substantial challenge.

To date, the most developed preparation approaches for $CsPbX_3$-based micro/nanostructures can be divided into two strategies: one is the liquid-phase method [14,18–20,38], and the other is the chemical vapor deposition (CVD) method [17,21–27,42]. Generally, the CVD route requires high temperature and an inert atmosphere, which need high energy consumption, a long preparation period, and effective waste management, and thus inevitably increase the cost and could limit the output in mass production. Recently, on the basis of the supersaturated recrystallization mechanism, Zheng *et al.* reported a low-temperature liquid-phase synthesis method to synthesize inner-defect-free inorganic perovskite $CsPbBr_3$ micro/nanoflake single crystals [44]. The very thin supersaturated solution layer serves to promote heterogeneous nucleation of the material on the substrate due to the lower activation energy for nucleation induced by the production of ordered adlayers of anions on the surface [45]. Recrystallization takes place upon liquid transfer, and the $CsPbX_3$ nanocrystals grow rapidly due to the presence of the highly supersaturated state of the ions. Accordingly, the facile and high-compatibility liquid-phase self-assembly growth method based on the supersaturated recrystallization mechanism is very promising in achieving low-cost and environment-friendly $CsPbX_3$ micro/nanostructures [19,44].

In this work, we report unprecedented single-mode lasing with broad wavelength tunability in self-assembly $CsPbX_3$ microcavities, including microplates, microrods, and microcubes, over an ultrawide pumping wavelength range of 400–2300 nm at RT by using a modified low-temperature liquid-phase growth method. The as-grown microcrystals are single crystalline with well-formed facets and act as high-quality laser cavities. The superior frequency down- and upconversion single-mode lasing via one- to a giant five-photon absorption process demonstrates high multiphoton absorption (MPA) efficiency and excellent optical gain from the electron–hole plasma (EHP) state in the perovskite microcavities. By simple compositional modulation, high-quality single-mode lasing can be extended from blue-violet to green (427–543 nm) with low threshold and high stability. Additionally, the pump-wavelength-dependent lasing thresholds and the time-resolved kinetic emissions of the laser pulses are explored to reveal the physical mechanisms underlying the lasing behaviors.

2. EXPERIMENTAL SECTION

A. Synthesis Process of $CsPbX_3$ Single Microcrystals

The compounds $CsPbX_3$ single microcrystals were synthesized using a modified low-temperature liquid-phase growth method. Typically, the N, N′-dimethylformamide (DMF)–$CsPbCl_xBr_{3-x}$ solution was prepared by mixing CsX (X = Cl or Br, 99.99%, Aladdin) and PbX_2 (X = Cl or Br, 99.99%, Aladdin) powders with a suitable stoichiometric ratio in DMF solvent, while the DMF–$CsPbBr_xI_{3-x}$ ($x < 3$) solution was obtained by mixing CsX (X = Br or I, 99.99%, Aladdin), PbX_2 (X = Br or I, 99.99%, Aladdin), and additive β-cyclodextrin (β-CD, 99%, TCI) powders in DMF, and then we kept stirring for 4 h at a temperature of 80°C. Upon cooling to RT, a drop of the DMF–$CsPbCl_xBr_{3-x}$ solution (30 μL) was dispensed onto a Si, sapphire, or quartz substrate, which was preheated to a relatively low temperature (e.g., 40°C), and we kept the temperature unchanged to evaporate the solvent at a controllable rate. After the DMF solvent completely evaporated, high-quality $CsPbCl_xBr_{3-x}$ single microcrystals with microplate, microrod, or microcube geometries were achieved on the substrate. In the contrary, $CsPbBr_xI_{3-x}$ microcrystals were synthesized by directly dropping the DMF–$CsPbBr_xI_{3-x}$ solution with β-CD (30 μL) onto the substrate, which was previously heated to a fairly high evaporation temperature of 330°C to ensure the perovskite crystals staying in the black cubic phase.

B. Characterization

Structural and morphological characterizations of the as-grown $CsPbX_3$ microcrystals were all conducted at RT (20°C). The

crystal phase of the investigated samples was investigated using an X-ray diffraction (XRD) spectrometer, (Cu Kα, D8-Avance, BrukerAXS, Germany). The morphology micrographs and the elemental analysis of the microcrystals were carried out using a high-resolution scanning electron microscope (SEM) with an energy-dispersive X-ray spectroscopy (EDS) system (XL30, Philips, the Netherlands). The optical absorption spectroscopy was measured using a UV-Vis-NIR spectrophotometer (Cary 5000, Varian, America).

C. Optical Measurements

All the photoluminescence (PL), lasing, and time-resolved PL experiments were performed with the home-built confocal μ-PL system at RT by a Ti:sapphire femtosecond (fs) pulse laser operating at 800 nm (35 fs, 1 kHz, Verdi G8, Coherent, America). The impulsive 400 nm pulses were generated by frequency doubling the 800 nm fs pulses via a β-barium-borate (BBO) crystal, while the impulsive 1300, 1800, and 2300 nm pulses were generated from an optical parametric amplifier (OPA) system pumped by the 800 nm fs pulses. The pump laser beam was introduced into the confocal system and focused to a spot through a 40× objective lens. The time-resolved kinetic investigation on pulse laser outputs was carried out by a streak-camera system (C10910, Hamamatsu, Japan) with a temporal resolution of about 10 ps. The luminescence signals were dispersed by a triple-grating spectrometer (Shamrock SR-303, Andor) and were recorded by a cooled charge-coupled device (CCD) camera.

3. RESULTS AND DISCUSSION

A. Direct Synthesis and Characterizations of CsPbX$_3$ Single Microcrystals

The schematic diagram of facile liquid-phase synthetic strategy for high-quality CsPbX$_3$ single microcrystals is presented in Fig. 1. Briefly, a drop of solution (~30 μL) containing dissolved solvent (CsX and PbX$_2$ compounds with a target stoichiometric ratio) and DMF solvent is dispensed onto single-crystal Si, sapphire, amorphous quartz, or other substrates, which were preheated to a given temperature T_h (e.g., 40°C) by a heater in ambient atmosphere. After the solution spreads out naturally, the DMF solvent begins to evaporate due to the higher substrate temperature. As the DMF continues to evaporate, the solution gradually experiences a highly super-

saturated state. Once the supersaturation reaches the critical value for nucleation, the nuclei start to form on the substrate, and the concentration at the solid–liquid interface is reduced to the saturation concentration of the solution [45]. A concentration gradient is then established in the solution, which serves as the driving force for the ion or molecule diffusion that results in the continuous growth of the CsPbX$_3$ microcrystals until the DMF solvent completely evaporates. The crystal geometry and size, as well as chemical composition, can be controlled by adjusting the evaporation temperature, reactant concentration, substrate material, and stoichiometric ratio. The general chemical form of the perovskite CsPbX$_3$ structure is illustrated in Fig. 1(b).

Figures 2(a)–2(c) show the top-view SEM images of the self-assembled CsPbBr$_3$ single microcrystals based on the liquid-phase recrystallization on single-crystal Si, sapphire, and amorphous quartz substrates, respectively, with the reactant concentration of 40 mmol/L at a evaporation temperature of 40°C. It is seen that the end facets of the CsPbBr$_3$ crystals are smooth, which is critical for efficient emission confinement by a naturally forming high-quality optical cavity. Besides, it is found that the perovskite microcrystals on Si substrate tend to form rectangular microplates that are pressed to the substrate surface. In contrast, the CsPbX$_3$ perovskites show microrod geometry on sapphire, while tilted microcubes appear on amorphous quartz under the same synthesis condition. By simply varying the halide composition, CsPbCl$_x$Br$_{3-x}$ single microcrystals with the abovementioned three geometries can be easily obtained. The chemical composition and uniform spatial distribution of corresponding elements over the whole crystals, e.g., CsPbCl$_3$ or CsPbBr$_3$, are confirmed by EDS mapping as shown in Figs. 2(e) and 2(f). The EDS analysis indicates that the atomic ratios of Cs/Pb/Cl and Cs/Pb/Br are respectively 1.06:1.02:2.92 and 0.96:0.96:3.08 [Fig. 2(d)], which are in good agreement with the ideal 1:1:3 stoichiometry of a CsPbX$_3$ crystal.

B. Broad Wavelength Tunable Emission from CsPbX$_3$ Microcrystals

Through direct compositional modulations, the band-gap energies and emission spectra of the CsPbX$_3$ microcrystals can be tuned over the entire visible spectral region from 420 nm (blue-violet) to 710 nm (red) [Fig. 3(a)]. The corresponding linear
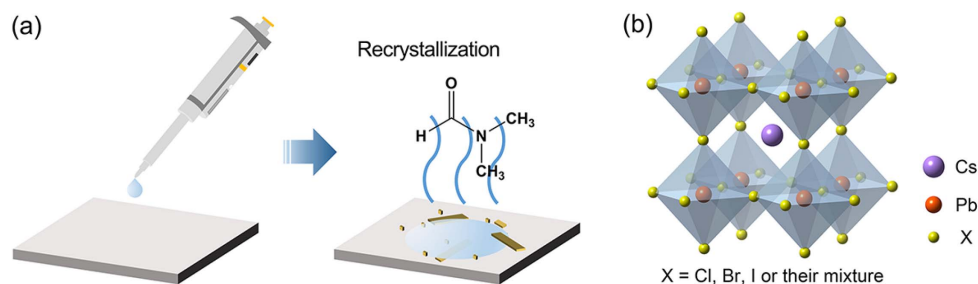

Fig. 1. Preparation of CsPbX$_3$ single microcrystals. (a) Illustration of the synthesis of CsPbX$_3$ microcrystals by the liquid-phase method. First, drop a certain amount of DMF–CsPbX$_3$ solution onto the substrate, which was preheated to a given temperature T_h, and keep the temperature unchanged in ambient air. Then, evaporate the DMF solvent under the given temperature (T_h). The solution gradually reaches supersaturation, and the nuclei start to form on the substrate. After the solvent is completely evaporated, the CsPbX$_3$ perovskite single microcrystals are obtained on the substrate surface. (b) Schematic chemical form of perovskite CsPbX$_3$ structure.
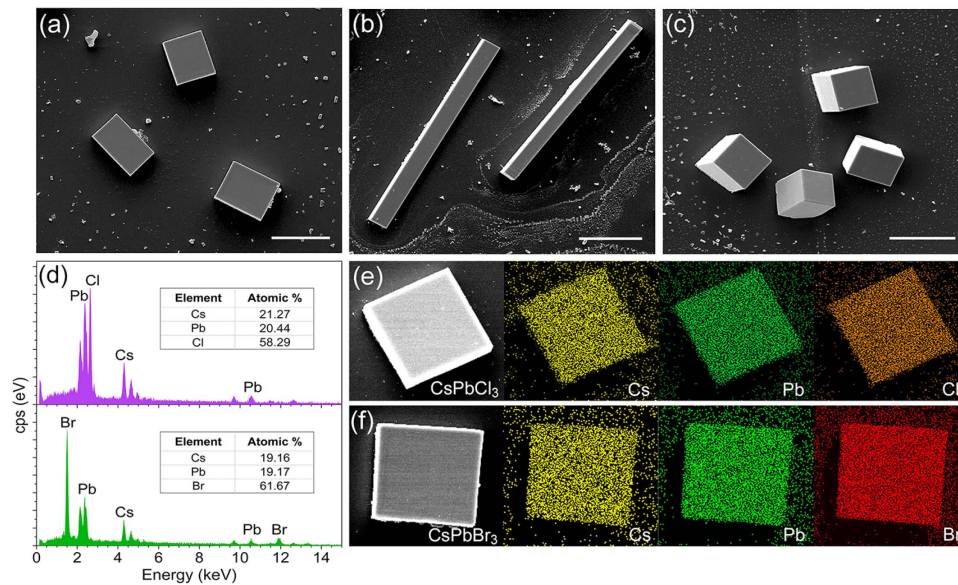
Fig. 2. Geometry of the CsPbCl$_x$Br$_{3-x}$ single microcrystals on different substrates. SEM micrograph of CsPbBr$_3$ on (a) single-crystal Si, (b) sapphire, and (c) amorphous quartz, with the reactant concentration of 40 mmol/L at an evaporation temperature of 40°C. Scale bars: 50 μm. (d) EDS spectra of the CsPbCl$_3$ and CsPbBr$_3$ microplates. Inset: atomic ratios of Cs/Pb/Cl and Cs/Pb/Br (~1:1:3). (e), (f) EDS elemental mapping of the corresponding CsPbCl$_3$ and CsPbBr$_3$ microplates, respectively.

optical absorption spectra of pure CsPbCl$_3$, CsPbBr$_3$, and CsPbI$_3$ crystals are concomitantly presented. The PL experiments were conducted under low excitation intensity at RT by fs impulsive optical pumping at 400 nm, namely, a frequency downconversion (one-photon absorption, 1PA) PL process, as illustrated in Fig. 3(b). Notably, the CsPbI$_3$ crystal increase, and then the valence and conduction (δ) phase with a wide band gap (~2.82 eV) at RT, while a preferred black cubic (α) perovskite phase with a narrow band gap (~1.73 eV) requires high temperature atmospheres (>310°C) [46,47]. Upon cooling, the cubic α-CsPbI$_3$ undergoes immediate transformation to the orthorhombic phase when exposed to ambient conditions [48]. Such intrinsic lack of stability is due to auto-degradation and susceptibility to hydrolysis from atmospheric water and oxygen [49,50]. To achieve cubic α-CsPbBr$_x$I$_{3-x}$ ($x < 3$) crystals with high phase stability, the supramolecular β-CD is introduced into the DMF–CsPbBr$_x$I$_{3-x}$ precursor solution prior to thermal evaporation at 330°C. After cooling to RT, the CsPbBr$_x$I$_{3-x}$ crystals with β-CD remain "frozen" in the black photoactive phase due to the drastically enhanced framework of the synthesized CsPbBr$_x$I$_{3-x}$ perovskites through the supramolecular interaction [51,52]. Such beneficial interaction tremendously improves the crystalline properties, humidity stability, and illumination stability of the perovskite materials. The molecular structure and approximate hydrophobic-cavity dimensions, as well as the schematic of the water-resistant property of the perovskite with β-CD, are respectively displayed in Figs. 3(c) and 3(d). Remarkably, such a new class of promoter for perovskite formation demonstrates the great potential of β-CD for a wide range of applications in perovskite-based optoelectronic devices, such as light-emitting diodes, lasers, and detectors. Figure 3(e) shows the XRD pattern evolution of the CsPbX$_3$ microcrystals with varying stoichiometric ratio

of halide ions (e.g., Cl/Br and Br/I ratios). By comparing the measured XRD patterns with the standard XRD patterns of cubic and orthorhombic CsPbX$_3$, it is found that the CsPbCl$_x$Br$_{3-x}$ possesses the orthorhombic crystal phase, showing observable peak splitting, while the CsPbBr$_x$I$_{3-x}$ counterparts exhibit the cubic crystal phase. The identifiable blueshifts of the diffraction peaks from CsPbCl$_3$ to CsPbI$_3$ are caused by the increasing lattice constant [20]. When the halide elemental weight increases from Cl to I, the energies of the halide p orbital increase, and then the valence and conduction bands move closer [21], leading to the decrease of optical band gap from ~2.95 eV (420 nm, CsPbCl$_3$) to ~1.75 eV (710 nm, CsPbI$_3$). The band-gap variations of the CsPbX$_3$ microcrystals are plotted in Fig. 4(f) as a function of chemical composition. By linearly fitting the experimental data, the dependence of band gap on composition (x) for the CsPbX$_3$ crystals can be quantitatively obtained as follows:

$$E_g[\text{CsPb}(\text{Cl}_x\text{Br}_{1-x})_3] = 2.332 + 0.604x \text{ (eV)}, \quad \text{(1)}$$

$$E_g[\text{CsPb}(\text{Br}_x\text{I}_{1-x})_3] = 1.691 + 0.641x \text{ (eV)}. \quad \text{(2)}$$

C. Robust Single-Mode Lasing from CsPbCl$_x$Br$_{3-x}$ Microcavities Based on 1PA

The as-grown microcrystals are directly used for lasing experiments without transferring them to other substrate by a micromanipulator. Owing to the excellent crystal quality and intrinsic high material gain, single-mode lasing from CsPbBr$_3$ microplates, microrods, and microcubes is successfully demonstrated under impulsive pumping at 400 nm. The pump laser beam is introduced into the confocal system and focused to a spot with the beam waist adjusted to be larger than the crystal facets using a 40× objective lens. The end facets
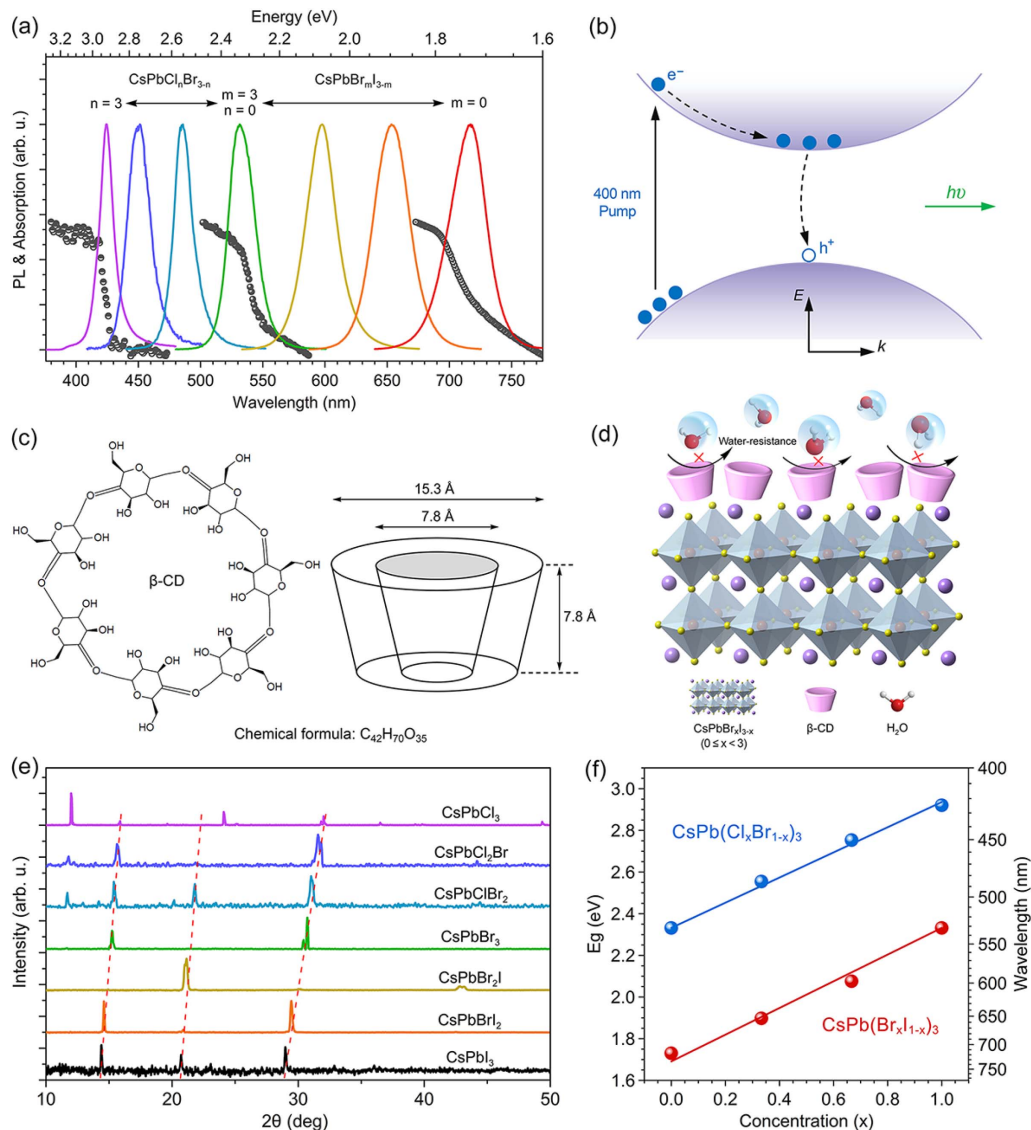
Fig. 3. Tunable band-gap energies and emission spectra of the $CsPbX_3$ microcrystals. (a) Tunable emission wavelength and absorption of the $CsPbX_3$ (X = Cl, Cl/Br, Br, Br/I, and I) mixed halide systems. (b) Schematic of the frequency downconversion (1PA) PL process. (c) Molecular structure and approximate cavity dimensions of β-CD. (d) Schematic diagram to show the mechanism for the water-resistant property of the $CsPbBr_xI_{3-x}$ ($0 \leq x < 3$) with β-CD. (e) XRD patterns of the as-grown $CsPbX_3$ mixed halide perovskites. (f) Band gaps of the $CsPbX_3$ with composition x. The filled circles are the experimental data, and the solid lines are the linearly fitted curves.

of these crystals naturally form a high-quality FP cavity or WGM cavity for optical amplification and oscillations. Under high pump fluence, along with the carrier density in the cavity achieving population inversion, amplified stimulated emission can be established. The lasing spectra and corresponding fluorescence microscopy images (see the insets) are shown in Figs. 4(a)–4(c) for the microplate, microrod, and microcube, respectively. The bright emission localized at the ends is consistent with a strong waveguiding effect and directly indicates that these microcrystals themselves form high-quality optical cavities. Figure 4(d) plots the representative integrated emission intensities (on log–log scales) and the full width at half-maximum (FWHM) as a function of pump fluence (P). The light input–light output (L–L) behaviors exhibit the typical "s-shaped" nonlinear characteristic of the transition

from original spontaneous emission (SPE) to stimulated emission with the increase of excitation intensity. The laser threshold is derived at about 24.1 $\mu J/cm^2$, which is comparable to those reported in previous works [25,53]. Meanwhile, an abrupt narrowing of the spectral linewidth is clearly seen due to spontaneous coherence buildup in the microcavity for the lasing onset. As the excitation density increases above ~ 35.2 $\mu J/cm^2$, the lasing intensity increases slowly due to gain saturation. The difference between the heights of the emission intensities before and after lasing roughly corresponds to an SPE coupling factor of ~ 0.05, which physically represents the coupling efficiency of the SPE to the lasing mode [54]. Note that this value of factor is comparable to those reported in well-known vertical-cavity surface-emitting lasers [55,56], indicating the efficient enhancement of the SPE into a lasing
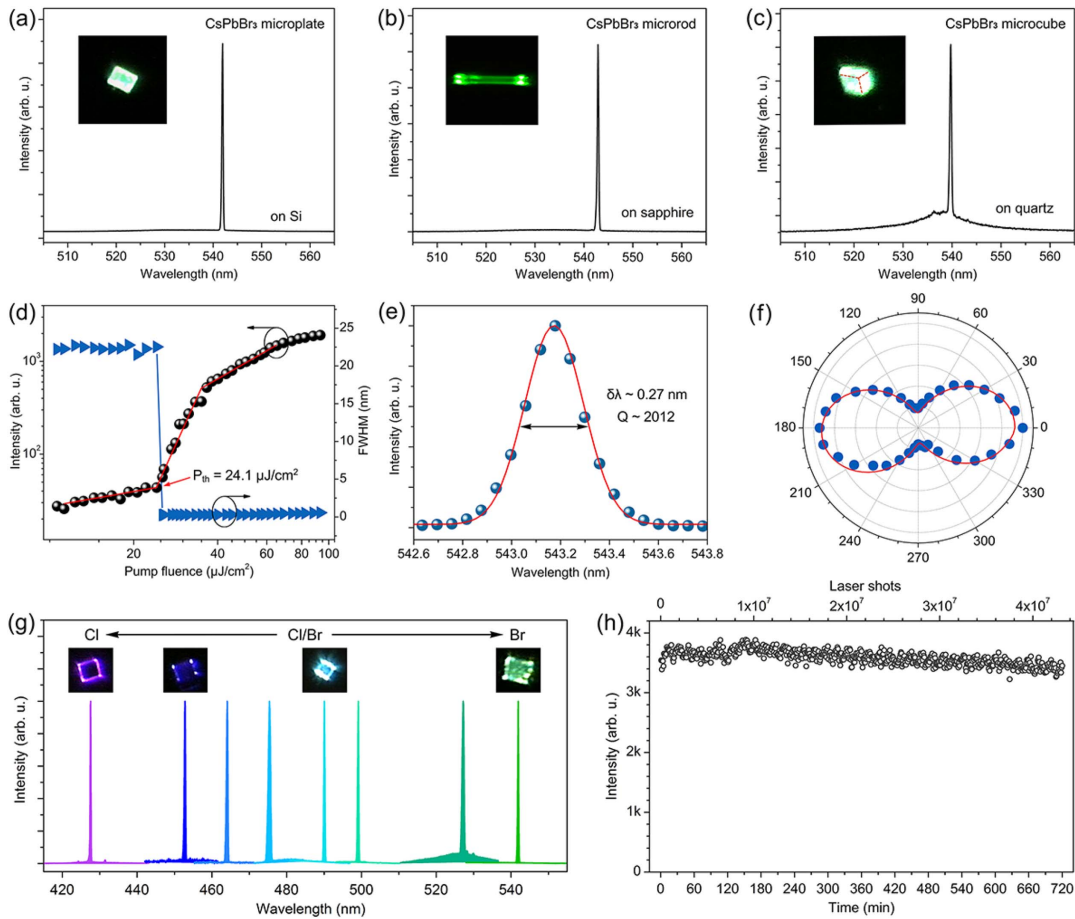
Fig. 4. Frequency downconversion single-mode lasing from CsPbCl$_x$Br$_{3-x}$ microcavities based on 1PA. Single-mode lasing of the CsPbBr$_3$ (a) microplate, (b) microrod, and (c) microcube. Insets: corresponding fluorescence microscopy images of the CsPbBr$_3$ microcrystals. (d) Integrated emission intensity and FWHM as a function of pump fluence showing the lasing threshold at ~24.1 µJ/cm^2 and gain saturation at ~35.2 µJ/cm^2. (e) Gaussian fitting of the lasing mode near the threshold, giving the FWHM of the lasing peak ($\delta\lambda$) ~0.27 nm and the Q factor ~2012. (f) Polarization characteristics of the laser emission at a pump fluence of 1.3P_{th}. The DOP is estimated to be 73%, corresponding to an orthogonal polarization suppression ratio of 16 dB. (g) Multicolor single-mode laser emissions and corresponding fluorescence microscopy images of the CsPbCl$_x$Br$_{3-x}$ microcrystals. (h) Integrated emission intensity of a CsPbBr$_3$ microplate under 400 nm fs laser excitation at a constant pump density of 1.5P_{th} for over 12 h while exposed to ambient atmosphere.

mode by the microcavity effect in the crystals. By well fitting the data with a Gaussian function, the lasing peak linewidth can be identified as 0.27 nm [Fig. 4(e)]. The cavity quality factor Q is then calculated to be ~2012 according to the relationship of $Q = \lambda/\delta\lambda$ [14], where λ is the peak center wavelength and $\delta\lambda$ is the peak width. Figure 4(f) depicts the polarization characteristics of the laser pulses. The integrated emission intensities are plotted as a function of detection polarization angle φ while keeping the pump fluence at 1.3P_{th} and fitted with a $\cos^2\varphi$ function. The degree of polarization (DOP), given by [57]

$$\text{DOP} = \frac{L_{\text{max}} - L_{\text{min}}}{L_{\text{max}} + L_{\text{min}}}, \qquad (3)$$

where L_{max} and L_{min} are respectively the maximum and minimum relative light intensities, is estimated to be 73%, showing a highly polarized excitation response with an orthogonal polarization suppression ratio of 16 dB [58,59]. Additionally,

by mixing different amounts of cesium bromide and chloride in the precursor solution, we have realized high-quality single-mode laser emission from CsPbCl$_x$Br$_{3-x}$ microcrystals over the spectral range from blue-violet to green (427–543 nm) as shown in Fig. 4(g). Note that the lasing operation is hardly achieved for the CsPbBr$_x$I$_{3-x}$ mixed halide system due to the irregularity in crystal morphology at a high synthesis temperature of 330°C. Besides, the additive β-CD may possibly enhance the light scattering and thus destroys the phase coherence of photons in the crystal. Nevertheless, the CsPbBr$_x$I$_{3-x}$ crystals with β-CD present substantially improved water stability and illumination stability, which are unattainable by conventional methods, and should be very valuable in a wide variety of new application areas, especially for high-efficiency light-emitting devices and solar cells [60,61]. To probe the stability of lasing outputs, the CsPbBr$_3$ microplate was constantly pumped by the 400 nm fs laser source with 35 fs duration and 1 kHz repetition rate in the ambient atmosphere (20°C, 45% relative

humidity) at $1.5P_{th}$ for over 12 h (up to 4.3×10^7 excitation cycles). As shown in Fig. 4(h), the laser emission remains stable and robust after long-term high-intensity excitation, demonstrating that the $CsPbX_3$ microlasers have great potential for integration onto on-chip optoelectronic circuitry.

D. Superior Frequency Upconversion Single-Mode Lasing from $CsPbCl_xBr_{3-x}$ Microcavities Based on MPA

MPA processes enable many technologically important applications such as biomedical imaging [62,63], photodynamic therapy [64], and optical limiting [65]. During the past few years, MPA upconversion luminescence and lasing for perovskite materials have received extensive attention, and the $CsPbBr_3$ nanocrystals and bulk phase materials have already been experimentally confirmed to be efficient multiphoton materials with large absorption cross sections [66] and resonantly enhanced multiple exciton generation [67]. However, up to now, although two- and three-photon absorption (2PA and 3PA) upconverted lasing has been recently achieved in all-inorganic perovskite micro/nanocavities [39–42], higher-order nonlinear absorption (e.g., 4PA or 5PA) laser action has been rarely reported despite the tremendous efforts. Here we first

demonstrate the amazing excellent frequency-upconverted single-mode lasing from the $CsPbCl_xBr_{3-x}$ microcrystals through 2PA to giant 5PA processes, covering an ultrawide pumping wavelength region of 800–2300 nm. Figure 5(a) shows the variation of emission spectra for the $CsPbBr_3$ microplate under progressively higher pump fluences. It is clearly seen that one single sharp peak abruptly appeared above the SPE background and grew drastically with increasing pump density, and no other resonant peaks were found in this process. The distinct evolvement from SPE to stimulated emission indicates the achievement of an upconversion single-mode laser. The 2PA excitation process via virtual energy levels is schematically illustrated in the inset of Fig. 5(a). Figures 5(b) and 5(c) present the corresponding threshold behaviors of emission intensity and FWHM evolution, as well as the Gaussian fitting of the lasing linewidth, respectively. From the "s-shaped" $L–L$ curve and the fitting result, the 2PA lasing threshold can be derived as ~ 63.5 μJ/cm^2, and the lasing linewidth is about 0.28 nm. The cavity factor Q is then calculated to be ~ 1940, which is comparable to that of 1PA scheme. Figures 5(d)–5(f) show the 3PA, 4PA, and 5PA upconversion single-mode laser emissions for the $CsPbBr_3$ microplates that are pumped by
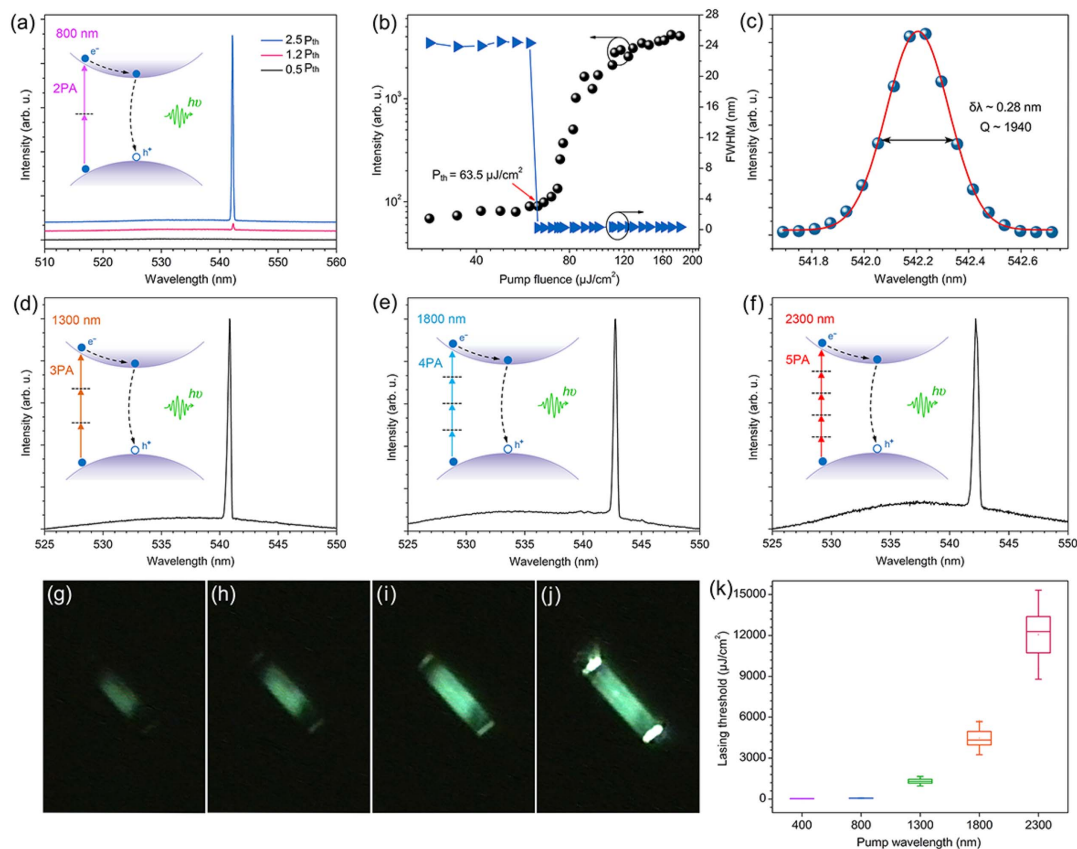

Fig. 5. Nonlinear frequency upconversion single-mode lasing from $CsPbX_3$ microcavities based on MPA. (a) Variation of the emission spectra for the $CsPbBr_3$ microplate pumped by 800 nm (2PA). (b) Integrated emission intensity and FWHM versus pump fluence, and (c) Gaussian fitting of the lasing mode at $1.1P_{th}$ based on 2PA. (d)–(f) Single-mode lasing from $CsPbBr_3$ microplate pumped by 1300 nm (3PA), 1800 nm (4PA), and 2300 nm (5PA), respectively. Insets: corresponding MPA and fluorescence mechanisms for the respective pump wavelengths. (g)–(j) Fluorescence microscopy images of the $CsPbBr_3$ microrod via 5PA with increasing pump fluence, showing the transition from original SPE to lasing. (k) Pump-wavelength-dependent lasing threshold of the $CsPbBr_3$ microrod.

1300, 1800, and 2300 nm, respectively, together with the corresponding MPA and fluorescence mechanisms (see the insets). Specifically, higher-order nonlinear absorption (4PA or 5PA) is especially desirable for next-generation multiphoton imaging due to its high spatial resolution, large penetration depth, and little photodamage and photobleaching [66,68]. Figures 5(g)–5(j) display the fluorescence microscopy images of a CsPbBr$_3$ microrod via 5PA with increasing pump fluence. As is shown, at excitation densities below the lasing threshold, SPE dominates, and the microrod is uniformly emissive. Upon surpassing the threshold, however, stimulated emission takes over, and the coherent emission from the two end facets is clearly observed, indicating a strong optical confinement effect in the microrod cavity. On the basis of the abovementioned experiments, the pump-wavelength dependence of the lasing threshold for the microrod via MPA is exhibited in Fig. 5(k). The statistical analysis reveals that the lasing threshold of the microrod is superlinearly increased with increasing pumping wavelength. The approximate values of the thresholds are 24.5 ± 4, 64.6 ± 10 μJ/cm², and 1.3 ± 0.2, 4.5 ± 0.7, 12 ± 2 mJ/cm² for the respective 400, 800, 1300, 1800, and 2300 nm excitations. Such superlinear increase of threshold can be ascribed to the relatively lower conversion efficiency due to higher-order nonlinear multiphoton effects [66,67].

Remarkably, despite this efficiency degeneration, the superior upconversion single-mode lasing has been unambiguously realized, for the first time, in all-inorganic microstructures via 2PA to giant 5PA processes, indicating excellent optical gain and efficient feedback within the microcavities. Further analysis of the carrier behaviors reveals that the formation of EHP in the cavity eventually contributes to the stimulated emission from the CsPbCl$_x$Br$_{3-x}$ microcrystals for the 1PA and MPA processes [39,69,70], which is discussed in more detail in Section 3.E.

E. Lasing Dynamics of Single-Mode Laser Pulses from CsPbCl$_x$Br$_{3-x}$ Microcavities

To gain additional insight into the lasing dynamics, time-resolved kinetic studies of pulse laser emission were performed using a streak-camera system. Figure 6(a) shows the representative streak-camera images of the detected PL from the CsPbBr$_3$ microplate when the excitation fluences are below ($0.8P_{th}$) and above ($1.6P_{th}$) the lasing threshold. It is clearly seen that, below the threshold, SPE with a broad emission band and longer decay time dominates the emission process, while a stimulated emission with a much narrower emission band and an ultrashort decay time dominates the process upon surpassing the threshold. Figure 6(b) plots the decay curves at the excitation densities of $0.5P_{th}$, $0.9P_{th}$, and $1.2P_{th}$, from which the
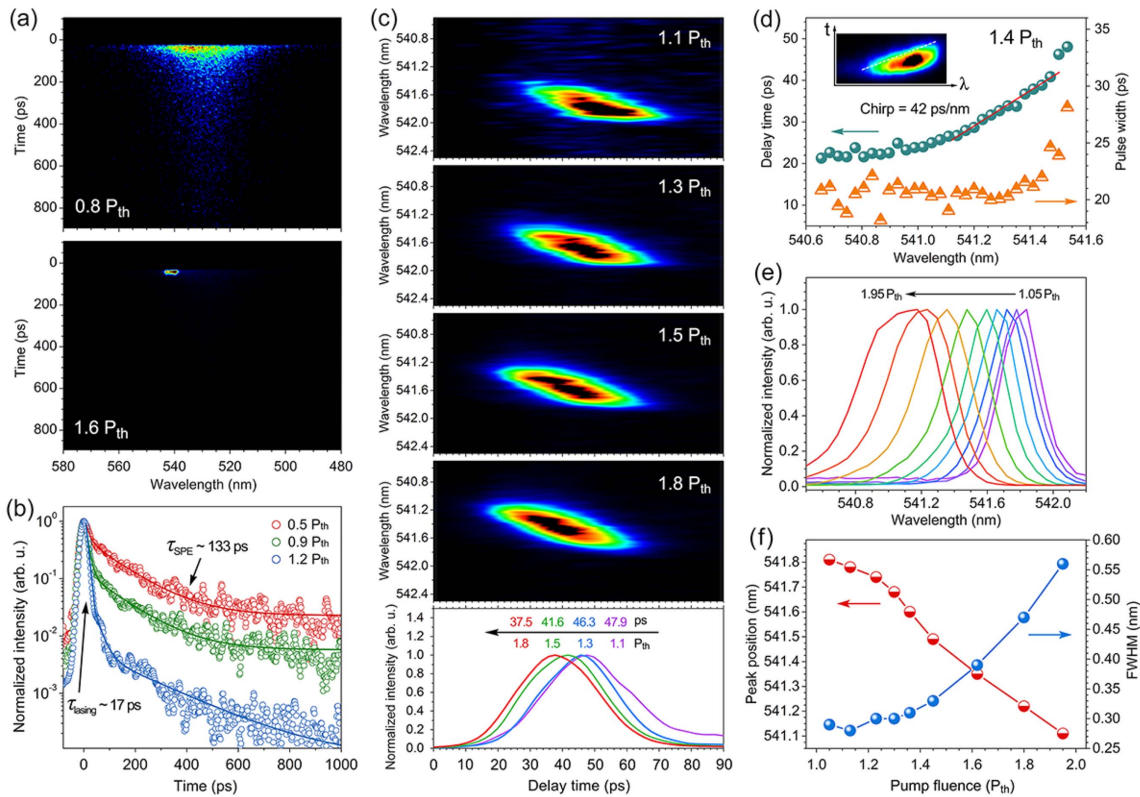

Fig. 6. Lasing dynamics of the CsPbX$_3$ microcavity lasers. (a) Streak-camera images of the CsPbBr$_3$ microplate at the pump densities of $0.8P_{th}$ (top panel) and $1.6P_{th}$ (bottom panel). (b) Typical PL decay curve obtained at three different excitation densities of $0.5P_{th}$, $0.9P_{th}$, and $1.2P_{th}$. (c) Streak-camera images and the corresponding spectral integrated waveforms of output pulses of gain-switched CsPbBr$_3$ microcavity lasers for various pump fluences. (d) Wavelength dependence of the delay time and pulse width of the laser outputs extracted from the streak-camera image (inset) with a pump density of $1.4P_{th}$. (e) Spectral evolution of the lasing pulses from the CsPbBr$_3$ microplate, showing the obvious peak blueshift and linewidth broadening with increasing pump fluences from $1.05P_{th}$ to $1.95P_{th}$. (f) Peak position and FWHM as a function of pump fluence extracted from (e).

lifetimes τ can be obtained through the exponential decay fitting. As is shown, the SPE lifetime is as long as ~133 ps at $0.5P_{th}$; with an increase of the pump density, a very fast decay with an ultrashort lifetime of 17 ps is observed above the threshold ($1.2P_{th}$), further manifesting the lasing occurrence in the microcavity. Moreover, the pump-density-dependent kinetic emission processes of the laser pulses above the lasing threshold are investigated to reveal the time-integrated spectral response of the perovskite microcavity. The streak-camera images and corresponding spectrally integrated waveforms of the pulses under progressively higher pump densities are shown in Fig. 6(c). As the pump fluence increases from $1.1P_{th}$ to $1.8P_{th}$, the delay time of the output pulse (or called laser onset time) is gradually reduced from 47.9 to 37.5 ps. At high excitations, the pump pulse is strong enough to enable carrier inversion in the $CsPbBr_3$ microlasers, whose initial distribution of photoexcited carriers depends on the pump power when the pump photon energy is fixed [71]. This nonequilibrium distribution relaxes by various interaction processes such as carrier–phonon interaction. The fast (~fs) energy redistribution with the hot electron (hole) gas causes almost a Fermi distribution with high electron (hole) temperatures much greater than the ambient temperature. The hot electrons and holes then equilibrate by interaction with the $CsPbBr_3$ lattice, mainly by carrier–phonon interactions [72]. Thus, the carrier relaxes to the respective band extremum by interactions with phonons, and the electrons and holes recombine by stimulated emission of photons with energies around the band-gap energy, which is therefore delayed relative to the pump pulse by a few picoseconds. Such onset time delay strongly depends on the pump power, that is, the onset delay of the stimulated emission decreases with increasing carrier density and saturates at a lower minimum when the carrier density is high enough that the spectral gain density becomes independent of any temporal carrier redistribution/relaxation close to the band gap. Conclusively, it is indeed an efficient way to tune the onset delay of $CsPbBr_3$ microlasers by directly modulating the pump power and the respective carrier density. This could also encourage more conceptual thinking for technologically relevant microlaser applications.

Figure 6(d) presents the wavelength dependence of pulse width and delay time of the output pulses at a pump density of $1.4P_{th}$. The delay time and pulse width at each wavelength are directly extracted from the streak-camera images (shown in the inset) for quantitative analysis. It is disclosed that, over the wavelength range from 541.1 to 541.5 nm, the delay time increases almost linearly with increasing wavelength (linear down chirp) with a slope (i.e., wavelength chirp) of 42 ps/nm. In the meanwhile, the pulse width for wavelengths below 541.3 nm remains almost constant at ~20 ps, while it gradually increases to ~28 ps with increasing wavelength for wavelengths longer than 541.3 nm. Actually, the reduction of delay time (laser onset time) at elevated excitation levels, the dependence of pulse width on wavelength, as well as the exponential rise and decay of the pulses are the typical characteristics of gain-switched pulses in semiconductor lasers [73,74]. Thanks to their outstanding optical gain, $CsPbX_3$ perovskites should be very fascinating for advancing the field of low-cost, compact, and

short-pulse semiconductor lasers based on the gain-switching technique for a variety of applications [75]. However, to the best of our knowledge, investigation on gain-switching characteristics in a perovskite laser is still lacking. Thus, great efforts should be devoted to both theoretical and experimental studies on this issue because of their significant academic and application value. Figures 6(e) and 6(f) show the variation of the normalized lasing spectra and corresponding peak position and FWHM with the increase of pump intensities, respectively. We can clearly identify the peak blueshifts and linewidth broadening with elevating pump levels, which can be unraveled by the chirping effect that results from changes in the carrier density and thus in the refractive index of the $CsPbBr_3$ matrix [74,76].

Based on the above results, the EHP mechanism is believed to be responsible for the stimulated emission in our $CsPbBr_3$ microcavities [19,39,69,70] because the formation of an EHP as the density of electron–hole pairs exceeds the Mott density (n_M) is expected to lead to a blueshift in the cavity modes due to a decrease in the refractive index that arises from exciton absorption saturation [77]. According to the previous systematic studies, the Mott density for $CsPbBr_3$ perovskites is reported from 1.8×10^{17} to 4.7×10^{17} cm^{-3} [19,21,70,78]. The carrier density (n_p) at the threshold of the $CsPbBr_3$ microplate in our system is estimated to be 3.7×10^{19} cm^{-3} by the relationship of [79]

$$n_p \approx \frac{\eta \cdot P_{exc}}{\hbar \omega_{exc} \cdot V}, \qquad (4)$$

where η is the PL quantum yield, P_{exc} the average excitation fluence, $\hbar$ the reduced Planck constant, ω_{exc} the angular frequency of excitation photon, and V the effective active volume of the $CsPbBr_3$. This value of n_p is almost 2 orders of magnitude higher than the reported Mott density, resulting in the stimulated emission from the EHP. Note that the lasing peak above the threshold appears only on the low-energy side of the PL spectrum, which further indicates the transition from the excitonic state to the EHP state that leads to the observed lasing, as reported for many other semiconductor nanostructures [80–83]. It is noteworthy that, for the multiphoton excitation conditions, the lasing thresholds are much higher than in the case of 1PA, as shown in Fig. 5(k), and thus the corresponding carrier density at the threshold far exceeds the Mott density for the MPA scenarios [84]. Consequently, we can reasonably conclude that the formation of EHP is the origin of the contribution from stimulated emission to optical gain in our $CsPbBr_3$ microcavities in the high-density regimes for both single- and multiphoton excitations.

4. CONCLUSION

In summary, we have realized unprecedented single-mode laser operations at RT in self-assembly $CsPbX_3$ single microcrystals (including microplate, microrod, and microcube geometries) over an ultrawide pumping wavelength region of 400–2300 nm, covering 1PA to 5PA processes. The as-grown microcrystals are single crystalline with well-formed facets and act as high-quality FP or WGM optical cavities. The higher-order nonlinear absorption (4PA or 5PA) single-mode laser action

manifests high MPA efficiency, efficient feedback, and excellent optical gain in the perovskite microcavities. The superlinear increase in lasing threshold for the microstructures with increasing pumping wavelengths is mainly attributed to the relatively lower conversion efficiency induced by higher-order nonlinear multiphoton effects. Through direct compositional modulation, the single-mode lasing emission can be continuously tuned from blue-violet to green (427–543 nm) with low threshold and high stability. The time-resolved kinetic studies of pulse laser emission provide additional insight into the lasing dynamics, including gain-switching and chirp characteristics, and the EHP recombination is considered the most convincing mechanism for the stimulated emission in the $CsPbX_3$ microcavities. These results suggest that self-assembly $CsPbX_3$ microcavities could be more promising and fascinating candidates for use in versatile optoelectronic integrated devices.

Disclosures. The authors declare no conflicts of interest.

†These authors contributed equally to this paper.

REFERENCES

1. M. S. Gudiksen, L. J. Lauhon, J. Wang, D. C. Smith, and C. M. Lieber, "Growth of nanowire superlattice structures for nanoscale photonics and electronics," Nature **415**, 617–620 (2002).
2. X. Duan, Y. Huang, R. Agarwal, and C. M. Lieber, "Single-nanowire electrically driven lasers," Nature **421**, 241–245 (2003).
3. R. Yan, D. Gargas, and P. Yang, "Nanowire photonics," Nat. Photonics **3**, 569–576 (2009).
4. Y. Li, Y. Zhang, L. Zhang, and A. W. Poon, "Silicon and hybrid silicon photonic devices for intra-datacenter applications: state of the art and perspectives," Photon. Res. **3**, B10–B27 (2015).
5. E. Knill, R. Laflamme, and G. J. Milburn, "A scheme for efficient quantum computation with linear optics," Nature **409**, 46–52 (2001).
6. W. W. Chow, F. Jahnke, and C. Gies, "Emission properties of nanolasers during the transition to lasing," Light Sci. Appl. **3**, e201 (2014).
7. R. Yan, J.-H. Park, Y. Choi, C.-J. Heo, S.-M. Yang, L. P. Lee, and P. Yang, "Nanowire-based single-cell endoscopy," Nat. Nanotechnol. **7**, 191–196 (2012).
8. K. Wang, G. Li, S. Wang, S. Liu, W. Sun, C. Huang, Y. Wang, Q. Song, and S. Xiao, "Dark-field sensors based on organometallic halide perovskite microlasers," Adv. Mater. **30**, 1801481 (2018).
9. Y. Nakayama, P. J. Pauzauskie, A. Radenovic, R. M. Onorato, R. J. Saykally, J. Liphardt, and P. Yang, "Tunable nanowire nonlinear optical probe," Nature **447**, 1098–1101 (2007).
10. K. Wang, S. Wang, S. Xiao, N. Zhang, Y. J. Wang, W. Yang, Y. H. Wang, C. Zhang, W. Sun, and Q. Song, "Single-crystalline perovskite microlasers for high-contrast and sub-diffraction imaging," Adv. Funct. Mater. **29**, 1904868 (2019).
11. L. Pan and D. B. Bogy, "Data storage: heat-assisted magnetic recording," Nat. Photonics **3**, 189–190 (2009).
12. S. W. Eaton, A. Fu, A. B. Wong, C.-Z. Ning, and P. Yang, "Semiconductor nanowire lasers," Nat. Rev. Mater. **1**, 16028 (2016).
13. Q. Zhang, S. T. Ha, X. Liu, T. C. Sum, and Q. Xiong, "Room-temperature near-infrared high-Q perovskite whispering-gallery planar nanolasers," Nano Lett. **14**, 5995–6001 (2014).
14. H. Zhu, Y. Fu, F. Meng, X. Wu, Z. Gong, Q. Ding, M. V. Gustafsson, M. T. Trinh, S. Jin, and X.-Y. Zhu, "Lead halide perovskite nanowire lasers with low lasing thresholds and high quality factors," Nat. Mater. **14**, 636–642 (2015).
15. B. R. Sutherland, S. Hoogland, M. M. Adachi, C. T. O. Wong, and E. H. Sargent, "Conformal organohalide perovskites enable lasing on spherical resonators," ACS Nano **8**, 10947–10952 (2014).
16. F. Deschler, M. Price, S. Pathak, L. E. Klintberg, D.-D. Jarausch, R. Higler, S. Hüttner, T. Leijtens, S. D. Stranks, H. J. Snaith, M. Atatüre, R. T. Phillips, and R. H. Friend, "High photoluminescence efficiency and optically pumped lasing in solution-processed mixed halide perovskite semiconductors," J. Phys. Chem. Lett. **5**, 1421–1426 (2014).
17. J. Xing, X. F. Liu, Q. Zhang, S. T. Ha, Y. W. Yuan, C. Shen, T. C. Sum, and Q. Xiong, "Vapor phase synthesis of organometal halide perovskite nanowires for tunable room-temperature nanolasers," Nano Lett. **15**, 4571–4577 (2015).
18. P. Liu, X. He, J. Ren, Q. Liao, J. Yao, and H. Fu, "Organic-inorganic hybrid perovskite nanowire laser arrays," ACS Nano **11**, 5766–5773 (2017).
19. S. W. Eaton, M. Lai, N. A. Gibson, A. B. Wong, L. Dou, J. Ma, L.-W. Wang, S. R. Leone, and P. Yang, "Lasing in robust cesium lead halide perovskite nanowires," Proc. Natl. Acad. Sci. USA **113**, 1993–1998 (2016).
20. Y. Fu, H. Zhu, C. C. Stoumpos, Q. Ding, J. Wang, M. G. Kanatzidis, X. Zhu, and S. Jin, "Broad wavelength tunable robust lasing from single-crystal nanowires of cesium lead halide perovskites ($CsPbX_3$, X = Cl, Br, I)," ACS Nano **10**, 7963–7972 (2016).
21. Q. Zhang, R. Su, X. Liu, J. Xing, T. C. Sum, and Q. Xiong, "High-quality whispering-gallery-mode lasing from cesium lead halide perovskite nanoplatelets," Adv. Funct. Mater. **26**, 6238–6245 (2016).
22. Y. Wang, X. Guan, D. Li, H.-C. Cheng, X. Duan, Z. Lin, and X. Duan, "Chemical vapor deposition growth of single-crystalline cesium lead halide microplatelets and heterostructures for optoelectronic applications," Nano Res. **10**, 1223–1233 (2017).
23. B. Tang, H. Dong, L. Sun, W. Zheng, Q. Wang, F. Sun, X. Jiang, A. Pan, and L. Zhang, "Single-mode lasers based on cesium lead halide perovskite submicron spheres," ACS Nano **11**, 10681–10688 (2017).
24. H. Zhou, S. Yuan, X. Wang, T. Xu, X. Wang, H. Li, W. Zheng, P. Fan, Y. Li, L. Sun, and A. Pan, "Vapor growth and tunable lasing of band gap engineered cesium lead halide perovskite micro/nanorods with triangular cross section," ACS Nano **11**, 1189–1195 (2017).
25. B. Zhou, H. Dong, M. Jiang, W. Zheng, L. Sun, B. Zhao, B. Tang, A. Pan, and L. Zhang, "Single-mode lasing and 3D confinement from perovskite micro-cubic cavity," J. Mater. Chem. C **6**, 11740–11748 (2018).
26. X. X. Wang, H. Chen, H. Zhou, X. Wang, S. Yuan, Z. Yang, X. Zhu, R. Ma, and A. Pan, "Room-temperature high-performance $CsPbBr_3$ perovskite tetrahedral microlasers," Nanoscale **11**, 2393–2400 (2019).
27. H. Zhang, C. Zhao, S. J. Chen, J. Tian, J. Yan, G. Weng, X. Hu, J. Tao, Y. Pan, S. Q. Chen, H. Akiyama, and J. Chu, "Lasing operation in the $CsPbBr_3$ perovskite micron hemisphere cavity grown by chemical vapor deposition," Chem. Eng. J. **389**, 124395 (2020).
28. H. He, E. Ma, X. Chen, D. Yang, B. Chen, and G. Qian, "Single crystal perovskite microplate for high-order multiphoton excitation," Small Methods **3**, 1900396 (2019).
29. K. Wang, W. Sun, S. Wang, S. Liu, N. Zhang, S. Xiao, and Q. Song, "Single crystal microrod based homonuclear photonic molecule lasers," Adv. Opt. Mater. **5**, 1600744 (2017).
30. Q. Wei, X. Li, C. Liang, Z. Zhang, J. Guo, G. Hong, G. Xing, and W. Huang, "Recent progress in metal halide perovskite micro- and nanolasers," Adv. Opt. Mater. **7**, 1900080 (2019).
31. Z. Liu, S. Huang, J. Du, C. Wang, and Y. Leng, "Advances in inorganic and hybrid perovskites for miniaturized lasers," Nanophotonics **9**, 2251–2272 (2020).
32. G. Xing, N. Mathews, S. S. Lim, N. Yantara, X. Liu, D. Sabba, M. Grätzel, S. Mhaisalkar, and T. C. Sum, "Low-temperature solution-processed wavelength-tunable perovskites for lasing," Nat. Mater. **13**, 476–480 (2014).

33. S. Yakunin, L. Protesescu, F. Krieg, M. I. Bodnarchuk, G. Nedelcu, M. Humer, G. D. Luca, M. Fiebig, W. Heiss, and M. V. Kovalenko, "Low-threshold amplified spontaneous emission and lasing from colloidal nanocrystals of caesium lead halide perovskites," Nat. Commun. **6**, 8056 (2015).

34. C. Qin, A. S. D. Sandanayaka, C. Zhao, T. Matsushima, D. Zhang, T. Fujihara, and C. Adachi, "Stable room-temperature continuous-wave lasing in quasi-2D perovskite films," Nature **585**, 53–57 (2020).

35. C. Huang, C. Zhang, S. Xiao, Y. Wang, Y. Fan, Y. Liu, N. Zhang, G. Qu, H. Ji, J. Han, L. Ge, Y. Kivshar, and Q. Song, "Ultrafast control of vortex microlasers," Science **367**, 1018–1021 (2020).

36. L. Protesescu, S. Yakunin, M. I. Bodnarchuk, F. Krieg, R. Caputo, C. H. Hendon, R. X. Yang, A. Walsh, and M. V. Kovalenko, "Nanocrystals of cesium lead halide perovskites (CsPbX₃, X = Cl, Br, and I): novel optoelectronic materials showing bright emission with wide color gamut," Nano Lett. **15**, 3692–3696 (2015).

37. Y. Wang, X. Li, J. Song, L. Xiao, H. Zeng, and H. Sun, "All-inorganic colloidal perovskite quantum dots: a new class of lasing materials with favorable characteristics," Adv. Mater. **27**, 7101–7108 (2015).

38. Y. Fu, H. Zhu, A. W. Schrader, D. Liang, Q. Ding, P. Joshi, L. Hwang, X.-Y. Zhu, and S. Jin, "Nanowire lasers of formamidinium lead halide perovskites and their stabilized alloys with improved stability," Nano Lett. **16**, 1000–1008 (2016).

39. X. X. Wang, H. Zhou, S. Yuan, W. Zheng, Y. Jiang, X. Zhuang, H. Liu, Q. Zhang, X. Zhu, X. Wang, and A. Pan, "Cesium lead halide perovskite triangular nanorods as high-gain medium and effective cavities for multiphoton-pumped lasing," Nano Res. **10**, 3385–3395 (2017).

40. Z. Liu, C. Wang, Z. Hu, J. Du, J. Yang, Z. Zhang, T. Shi, W. Liu, X. Tang, and Y. Leng, "Mode selection and high-quality upconversion lasing from perovskite CsPb₂Br₅ microplates," Photon. Res. **8**, A31–A38 (2020).

41. Z. Hu, Z. Liu, Y. Bian, D. Liu, X. Tang, W. Hu, Z. Zang, M. Zhou, L. Sun, J. Tang, Y. Li, J. Du, and Y. Leng, "Robust cesium lead halide perovskite microcubes for frequency upconversion lasing," Adv. Opt. Mater. **5**, 1700419 (2017).

42. B. Zhou, M. Jiang, H. Dong, W. Zheng, Y. Huang, J. Han, A. Pan, and L. Zhang, "High-temperature upconverted single-mode lasing in 3D fully inorganic perovskite microcubic cavity," ACS Photon. **6**, 793–801 (2019).

43. L. W. Casperson, "Threshold characteristics of multimode laser oscillators," J. Appl. Phys. **46**, 5194–5201 (1975).

44. W. Zheng, X. Xiong, R. Lin, Z. Zhang, C. Xu, and F. Huang, "Balanced photodetection in one-step liquid-phase-synthesized CsPbBr₃ micro-/nanoflake single crystals," ACS Appl. Mater. Interfaces **10**, 1865–1870 (2018).

45. M. V. Kelso, N. K. Mahenderkar, Q. Chen, J. Z. Tubbesing, and J. A. Switzer, "Spin coating epitaxial films," Science **364**, 166–169 (2019).

46. C. C. Stoumpos, C. D. Malliakas, and M. G. Kanatzidis, "Semiconducting tin and lead iodide perovskites with organic cations: phase transitions, high mobilities, and near-infrared photoluminescent properties," Inorg. Chem. **52**, 9019–9038 (2013).

47. G. E. Eperon, G. M. Paternò, R. J. Sutton, A. Zampetti, A. A. Haghighirad, F. Cacialli, and H. J. Snaith, "Inorganic caesium lead iodide perovskite solar cell," J. Mater. Chem. A **3**, 19688–19695 (2015).

48. A. Swarnkar, A. R. Marshall, E. M. Sanehira, B. D. Chernomordik, D. T. Moore, J. A. Christians, T. Chakrabarti, and J. M. Luther, "Quantum dot-induced phase stabilization of α-CsPbI₃ perovskite for high-efficiency photovoltaics," Science **354**, 92–95 (2016).

49. B. Conings, J. Drijkoningen, N. Gauquelin, A. Babayigit, J. D'Haen, L. D'Olieslaeger, A. Ethirajan, J. Verbeeck, J. Manca, E. Mosconi, F. De Angelis, and H.-G. Boyen, "Intrinsic thermal instability of methylammonium lead trihalide perovskite," Adv. Energy Mater. **5**, 1500477 (2015).

50. Y. Liao, H. Liu, W. Zhou, D. Yang, Y. Shang, Z. Shi, B. Li, X. Jiang, L. Zhang, L. N. Quan, R. Q. Bermudez, B. R. Sutherland, Q. Mi, E. H. Sargent, and Z. Ning, "Highly oriented low-dimensional tin halide perovskites with enhanced stability and photovoltaic performance," J. Am. Chem. Soc. **139**, 6693–6699 (2017).

51. S. Masi, F. Aiello, A. Listorti, F. Balzano, D. Altamura, C. Giannini, R. Caliandro, G. U. Barretta, A. Rizzo, and S. Colella, "Connecting the solution chemistry of PbI₂ and MAI: a cyclodextrin-based supramolecular approach to the formation of hybrid halide perovskites," Chem. Sci. **9**, 3200–3208 (2018).

52. D. Wei, H. Huang, P. Cui, J. Ji, S. Dou, E. Jia, S. Sajid, M. Cui, L. Chu, Y. Li, B. Jiang, and M. Li, "Moisture-tolerant supermolecule for the stability enhancement of organic-inorganic perovskite solar cells in ambient air," Nanoscale **11**, 1228–1235 (2019).

53. Z. Liu, J. Yang, J. Du, Z. Hu, T. Shi, Z. Zhang, Y. Liu, X. Tang, Y. Leng, and R. Li, "Robust subwavelength single-mode perovskite nanocuboid laser," ACS Nano **12**, 5923–5931 (2018).

54. S. Kreinberg, W. W. Chow, J. Wolters, C. Schneider, C. Gies, F. Jahnke, S. Höfling, M. Kamp, and S. Reitzenstein, "Emission from quantum-dot high-β microcavities: transition from spontaneous emission to lasing and the effects of superradiant emitter coupling," Light Sci. Appl. **6**, e17030 (2017).

55. T.-C. Lu, J.-R. Chen, S.-W. Chen, H.-C. Kuo, C.-C. Kuo, C.-C. Lee, and S.-C. Wang, "Development of GaN-based vertical-cavity surface-emitting lasers," IEEE J. Sel. Top. Quantum Electron. **15**, 850–860 (2009).

56. G. Weng, S. Chen, Y. Mei, Y. Liu, H. Akiyama, X. Hu, J. Liu, B. Zhang, and J. Chu, "Multiwavelength GaN-based surface-emitting lasers and their design principles," Ann. Phys. **532**, 1900308 (2020).

57. Y. Mei, G. Weng, B. Zhang, J. Liu, W. Hofmann, L. Ying, J. Zhang, Z. Li, H. Yang, and H.-C. Kuo, "Quantum dot vertical-cavity surface-emitting lasers covering the 'green gap'," Light Sci. Appl. **6**, e16199 (2017).

58. G. Weng, Y. Mei, J. Liu, W. Hofmann, L. Ying, J. Zhang, Y. Bu, Z. Li, H. Yang, and B. Zhang, "Low threshold continuous-wave lasing of yellow-green InGaN-QD vertical-cavity surface-emitting lasers," Opt. Express **24**, 15546–15553 (2016).

59. Y. Higuchi, K. Omae, H. Matsumura, and T. Mukai, "Room-temperature CW lasing of a GaN-based vertical-cavity surface-emitting laser by current injection," Appl. Phys. Express **1**, 121102 (2008).

60. L. N. Quan, B. P. Rand, R. H. Friend, S. G. Mhaisalkar, T.-W. Lee, and E. H. Sargent, "Perovskites for next-generation optical sources," Chem. Rev. **119**, 7444–7477 (2019).

61. M. A. Green, A. H. Baillie, and H. J. Snaith, "The emergence of perovskite solar cells," Nat. Photonics **8**, 506–514 (2014).

62. S. J. J. Kwok, N. Martino, P. H. Dannenberg, and S.-H. Yun, "Multiplexed laser particles for spatially resolved single-cell analysis," Light Sci. Appl. **8**, 74 (2019).

63. Y. Peng, W. Lu, P. Ren, Y. Ni, Y. Wang, L. Zhang, Y. Zeng, W. Zhang, and S. Ruan, "Integration of nanoscale light emitters: an efficient ultraviolet and blue random lasing from NaYF₄:Yb/Tm hexagonal nanocrystals," Photon. Res. **6**, 943–947 (2018).

64. P. Zhang, W. Steelant, M. Kumar, and M. Scholfield, "Versatile photosensitizers for photodynamic therapy at infrared excitation," J. Am. Chem. Soc. **129**, 4526–4527 (2007).

65. J. E. Ehrlich, X. L. Wu, I.-Y. S. Lee, Z.-Y. Hu, H. Röckel, S. R. Marder, and J. W. Perry, "Two-photon absorption and broadband optical limiting with bis-donor stilbenes," Opt. Lett. **22**, 1843–1845 (1997).

66. W. Chen, S. Bhaumik, S. A. Veldhuis, G. Xing, Q. Xu, M. Grätzel, S. Mhaisalkar, N. Mathews, and T. C. Sum, "Giant five-photon absorption from multidimensional core-shell halide perovskite colloidal nanocrystals," Nat. Commun. **8**, 15198 (2017).

67. A. Manzi, Y. Tong, J. Feucht, E.-P. Yao, L. Polavarapu, A. S. Urban, and J. Feldmann, "Resonantly enhanced multiple exciton generation through below-band-gap multi-photon absorption in perovskite nanocrystals," Nat. Commun. **9**, 1518 (2018).

68. J. H. Yu, S.-H. Kwon, Z. Petrášek, O. K. Park, S. W. Jun, K. Shin, M. Choi, Y. I. Park, K. Park, H. B. Na, N. Lee, D. W. Lee, J. H. Kim, P. Schwille, and T. Hyeon, "High-resolution three-photon biomedical imaging using doped ZnS nanocrystals," Nat. Mater. **12**, 359–366 (2013).

69. M. Saba, M. Cadelano, D. Marongiu, F. Chen, V. Sarritzu, N. Sestu, C. Figus, M. Aresti, R. Piras, A. G. Lehmann, C. Cannas, A. Musinu, F. Quochi, A. Mura, and G. Bongiovanni, "Correlated electron-hole plasma in organometal perovskites," Nat. Commun. **5**, 5049 (2014).

70. A. P. Schlaus, M. S. Spencer, K. Miyata, F. Liu, X. Wang, I. Datta, M. Lipson, A. Pan, and X.-Y. Zhu, "How lasing happens in CsPbBr₃ perovskite nanowires," Nat. Commun. **10**, 265 (2019).

71. R. Röder and C. Ronning, "Review on the dynamics of semiconductor nanowier lasers," Semicond. Sci. Technol. **33**, 033001 (2018).

72. J. Yang, X. Wen, H. Xia, R. Sheng, Q. Ma, J. Kim, P. Tapping, T. Harada, T. W. Kee, F. Huang, Y.-B. Cheng, M. Green, A. H. Baillie, S. Huang, S. Shrestha, R. Patterson, and G. Conibeer, "Acoustic-optical phonon up-conversion and hot-phonon bottleneck in lead-halide perovskites," Nat. Commun. **8**, 14120 (2017).

73. T. Ito, H. Nakamae, Y. Hazama, T. Nakamura, S. Chen, M. Yoshita, C. Kim, Y. Kobayashi, and H. Akiyama, "Femtosecond pulse generation beyond photon lifetime limit in gain-switched semiconductor lasers," Commun. Phys. **1**, 42 (2018).

74. S. Chen, T. Ito, A. Asahara, M. Yoshita, W. Liu, J. Zhang, B. Zhang, T. Suemoto, and H. Akiyama, "Spectral dynamics of picosecond gain-switched pulses from nitride-based vertical-cavity surface-emitting lasers," Sci. Rep. **4**, 4325 (2014).

75. G. Weng, J. Xue, J. Tian, X. Hu, X. Bao, H. Lin, S. Chen, Z. Zhu, and J. Chu, "Picosecond random lasing based on three-photon absorption in organometallic halide $CH_3NH_3PbBr_3$ perovskite thin films," ACS Photon. **5**, 2951–2959 (2018).

76. J. Tatebayashi, S. Kako, J. Ho, Y. Ota, S. Iwamoto, and Y. Arakawa, "Room-temperature lasing in a single nanowire with quantum dots," Nat. Photonics **9**, 501–505 (2015).

77. J. C. Johnson, H. Yan, P. Yang, and R. J. Saykally, "Optical cavity effects in ZnO nanowire lasers and waveguides," J. Phys. Chem. B **107**, 8816–8828 (2003).

78. A. P. Schlaus, M. S. Spencer, and X.-Y. Zhu, "Light-matter interaction and lasing in lead halide perovskites," Acc. Chem. Res. **52**, 2950–2959 (2019).

79. Q. Han, J. Wang, J. Lu, L. Sun, F. Lyu, H. Wang, Z. Chen, and Z. Wang, "Transition between exciton-polarition and coherent photonic lasing in all-inorganic perovskite microcuboid," ACS Photon. **7**, 454–462 (2020).

80. S. Mitsubori, I. Katayama, S. H. Lee, T. Yao, and J. Takeda, "Ultrafast lasing due to electron-hole plasma in ZnO nano-multipods," J. Phys. Condens. Matter **21**, 064211 (2009).

81. J. Dai, C. X. Xu, P. Wu, J. Y. Guo, Z. H. Li, and Z. L. Shi, "Exciton and electron-hole plasma lasing in ZnO dodecagonal whispering-gallery-mode microcavities at room temperature," Appl. Phys. Lett. **97**, 011101 (2010).

82. J. Fallert, F. Stelzl, H. Zhou, A. Reiser, K. Thonke, R. Sauer, C. Klingshirn, and H. Kalt, "Lasing dynamics in single ZnO nanorods," Opt. Express **16**, 1125–1131 (2008).

83. S. Peng, G. Xing, and Z. Tang, "Hot electron-hole plasma dynamics and amplified spontaneous emission in ZnTe nanowires," Nanoscale **9**, 15612–15621 (2017).

84. M. He, Y. Jiang, Q. Liu, Z. Luo, C. Ouyang, X. X. Wang, W. Zheng, K. Braun, A. J. Meixner, T. Gao, X. Wang, and A. Pan, "Revealing excitonic and electron-hole plasma states in stimulated emission of single $CsPbBr_3$ nanowires at room temperature," Phys. Rev. Appl. **13**, 044072 (2020).